



Cite this: DOI: 10.1039/c9ta00148d

# Engineering rGO nanosheets-adsorption layer supported Pt nanoparticles to enhance photo-thermal catalytic activity under light irradiation†

Juan-Juan Li,<sup>‡a</sup> Song-Cai Cai,<sup>‡ab</sup> Xi Chen,<sup>ab</sup> Dong-Xu Yan,<sup>ab</sup> Jing Chen<sup>idbc</sup> and Hong-Peng Jia<sup>id\*ab</sup>

The direct conversion of renewable clean solar energy into heat to drive various catalytic reactions, e.g., oxidative degradation of volatile organic compounds, is highly desirable but remains challenging because of its low efficiency. In this work, a Pt-decorated-rGO nanosheet adsorption layer is rationally fabricated to achieve highly selective conversion of gaseous toluene to carbon dioxide under light irradiation. Specifically, its maximum photo-thermal conversion efficiency reaches 17.6% with a significant toluene conversion of 98% and CO<sub>2</sub> yield of 96% under 146 mW cm<sup>-2</sup> infrared light irradiation, together with excellent stability of nearly 45 h, much superior to that of the previous reported catalyst of Pt-rGO-TiO<sub>2</sub>. The comparison characterizations evidence that this excellent performance is predominantly attributed to the synergistic effects of ultrabroadband strong IR light absorption, efficient light-to-heat conversion, well-dispersed active Pt nanoparticles and strong reactant adsorption capacity with light irradiation. This work highlights that rGO nanosheets-adsorption layer directs light harnessing, Pt nanoparticle dispersion and reactant adsorption, showing great promise for redox reactions through photo-thermal effect. It is anticipated that this study will provide insight into the design of more energy-efficient catalysts with significant utilization of solar energy.

Received 5th January 2019  
Accepted 9th April 2019

DOI: 10.1039/c9ta00148d

rsc.li/materials-a

## 1. Introduction

Catalysis is an extremely efficient approach for atmospheric degradation of volatile organic compounds. However, in the commercial heterogeneous catalytic reactions, a large amount of thermal energy is generally required from fossil-derived fuels and is characterized by low energy efficiency;<sup>1</sup> additionally, combustion of nonrenewable crude oil is associated with natural resource depletion and is causing the imminent energy crisis and irreversible environmental damage. The direct conversion of renewable clean solar energy into heat has been of tremendous research interest recently for a number of potential applications in solar power generation or seawater desalination, as well as in environmental catalysis.<sup>2-5</sup> Fundamentally, solar-to-heat energy conversion requires materials that have strong absorption capability spanning a broad spectrum and enable

forceful coupling of the harvested photons into thermal energy accessible to catalytic active sites for chemical reactions. Currently, a photothermal phenomenon powered by localized plasmon-mediated heating on the surfaces of noble metal nanoparticles (NPs) can be realized.<sup>6-8</sup> Despite these advancements, the reported metallic nanomaterials respond only to a limited range of the solar spectrum and usually have a low energy utilization efficiency, since the optical properties of these plasmonic nanomaterials across the entire solar spectrum critically depend on size, shape and composition.<sup>9</sup> It is still an important and challenging issue to improve solar-to-heat efficiency, especially in the infrared (IR) wavelength light that constitutes 53% of the solar energy reaching earth's surface.<sup>10</sup> The exploitation of catalysts that extend the light absorption from the UV-visible to IR regions always remains a high-priority target and can be done by narrowing the bandgap of the materials, based on the principle of the full utilization of solar light.<sup>11</sup>

Inspired by the observation of a surprisingly large infrared absorption band in reduced graphene oxide (rGO) originating from the coupling of electronic states to the asymmetric stretch mode,<sup>12</sup> there has been a resurgence of exploration of graphene-based photo-thermal responsive materials. Our recent study demonstrated that Pt-rGO-TiO<sub>2</sub> composite featuring a broad IR light wavelength absorption possesses the capability for remarkable photo-thermal catalytic activity under IR light irradiation, with its performance intensively correlated to the

<sup>a</sup>CAS Center for Excellence in Regional Atmospheric Environment, Key Laboratory of Urban Pollutant Conversion, Institute of Urban Environment, Chinese Academy of Sciences, Xiamen 361021, P. R. China. E-mail: hpjia@iue.ac.cn

<sup>b</sup>University of Chinese Academy of Sciences, Beijing, 100049, P. R. China

<sup>c</sup>Xiamen Institute of Rare-earth Materials, Haixi Institutes, Chinese Academy of Sciences, Xiamen, Fujian 361021, P. R. China

† Electronic supplementary information (ESI) available. See DOI: 10.1039/c9ta00148d

‡ These authors contributed equally to this work.

advisable introduction of few-layered rGO nanosheets which enhance light-to-heat conversion, improve reactant adsorption capacity and enable well-dispersed supported Pt-TiO<sub>2</sub> catalyst on the 2D rGO nanosheets.<sup>13</sup> Unfortunately, this photo-thermal catalyst suffered from moderate selective conversion of gaseous toluene to carbon dioxide under light irradiation, accompanied by generated recalcitrant carbonaceous intermediates possibly depositing/blocking/poisoning adsorption sites and catalytic active sites.<sup>14</sup> Accordingly, it remains a challenge but an opportunity to further search for a material that can thoroughly decompose organic pollutants into end-product CO<sub>2</sub>, especially in the IR-light region.

To get a more active catalyst, one needs to modulate the molecule-scale surface properties to fundamentally improve reactant adsorption, enhance light-to-heat temperature and expose a greater fraction of catalytic active sites. Specifically, adsorption of the reactant onto the catalyst, particularly at the light-induced temperature, needs to be carefully considered. Herein, we show that the rGO nanosheets-adsorption layer supported Pt NPs, characterized by excellent IR light absorption, efficient light-to-heat conversion, high reactant adsorption capacity and well-dispersed active Pt NPs, can convert solar light, especially a low-intensity IR photon flux, into heat to enhance catalytic activity. In particular, Pt-rGO hybrid displays high catalytic performance with 98% toluene conversion and 96% CO<sub>2</sub> yield under IR irradiation intensity of 146 mW cm<sup>-2</sup>, as well as excellent stability. It is anticipated that this work will open new avenues toward the design of more energy-efficient catalysts with significant utilization of inexhaustible solar energy.

## 2. Experimental

### 2.1. Preparation of graphene oxide

Graphene oxide (GO) was synthesized from natural graphite powder by a modified Hummers' method.<sup>15</sup> In detail, 2 g of graphite powder (Alfa Aesar) was put into a mixture of 50 mL concentrated H<sub>2</sub>SO<sub>4</sub> and 1 g NaNO<sub>3</sub> in an ice water bath, then 8 g of KMnO<sub>4</sub> was added gradually under vigorous stirring for 120 min. Then, the solution was heated to 35 °C in an oil-bath and kept stirring for 2 h. 50 mL of deionized (DI) water was added into the above mixture, followed by stirring at 95 °C for 0.5 h. Then, 50 mL of DI water and 20 mL of 30% H<sub>2</sub>O<sub>2</sub> were added to the resulting mixture to remove unreacted KMnO<sub>4</sub>. When cooled to room temperature, the supernatant underwent two high-speed centrifugation steps at 8000 rpm for 10 min each, then was washed with 5% HCl aqueous solution to remove metal ions followed by DI water to remove the acid. The product was ultrasonicated for 1.5 h, then stirred under ambient conditions overnight. The mixture was carefully diluted with deionized (DI) water, filtered, and washed until the pH of the rinse water became neutral. Finally, a homogeneous GO aqueous solution (4 mg mL<sup>-1</sup>) was obtained.

### 2.2. Preparation of Pt-rGO composite

To synthesize the Pt-reduced graphene oxide (Pt-rGO) composite, a simple solvothermal method using ethanol-water

as solvent was followed.<sup>16,17</sup> 40 mL of GO aqueous solution (4 mg mL<sup>-1</sup>) was ultrasonicated in 80 mL deionized water and 60 mL anhydrous ethanol solution to disperse it well; after that, 0.437 mL of H<sub>2</sub>PtCl<sub>6</sub> (3.8 mg mL<sup>-1</sup>) aqueous solution was rapidly injected by pipet into the above GO solution to prepare Pt-rGO nanocomposite catalyst. The mixing solution was aged with vigorous stirring for 2 h to obtain a homogeneous suspension. This suspension was transferred to a Teflon-sealed autoclave and maintained at 120 °C for 24 h. Under such solvothermal conditions, the ethanol-water solvent has strong power to simultaneously reduce Pt<sup>4+</sup> and GO into Pt and rGO. The resulting composites were filtered, washed with deionized water, and fully dried at 60 °C in a vacuum oven to get the final Pt-rGO composite.

For comparison, the preparation procedure of rGO was similar to that of Pt-rGO without addition of Pt solution.

### 2.3. Catalyst characterization

Powder X-ray diffraction (XRD) characterization was carried out on an X'Pert Pro automatic powder diffractometer operated at 40 kV and 40 mA using Cu K $\alpha$  monochromatized radiation. Raman spectroscopy was carried out on a LabRAM Aramis using a green laser of 532 nm wavelength. The actual loading content of noble metal was determined by inductively coupled plasma atomic emission spectroscopy (ICP-AES, Varian, VISTAMPX-ICP). Nitrogen adsorption-desorption measurements of the catalysts were performed on a Quantachrome Autosorb iQ2 adsorption automatic instrument at liquid nitrogen temperature. All samples were degassed under vacuum at 60 °C for 24 h before measurement. Diffuse reflectance spectra were recorded using a Varian Cary 5000 UV-vis spectrophotometer at room temperature with BaSO<sub>4</sub> as a reference. XPS analysis was conducted on a Thermo Scientific ESCALAB 250 with a monochromatised microfocused Al X-ray source. Transmission electron microscopy (TEM) was performed using a JEOL model JEM 2100 EX instrument at an acceleration voltage of 200 kV. Temperature-programmed desorption (TPD) measurement was performed on a Quantachrome Chemstar instrument as follows. 50 mg catalyst sample was placed in an adsorption vessel and pretreated in He flow (50 mL min<sup>-1</sup>) at 150 °C for 60 min, then cooled/heated to a specified temperature (25, 120, 150 and 180 °C) for 120 min in a flow of gaseous toluene (30 mL min<sup>-1</sup>). Then, the sample was swept with He for 60 min and heated to 600 °C at a rate of 10 °C min<sup>-1</sup> under a He flow of 30 mL min<sup>-1</sup>. The desorbed products were monitored simultaneously by mass spectroscopy. The specific heat capacity of the sample was obtained by differential scanning calorimeter (Netzsch STA 449C, Thermal Analysis Corporation, Germany) from 30 to 300 °C at a heating rate of 5 °C min<sup>-1</sup> under an air flow of 50 mL min<sup>-1</sup>. *In situ* DRIFTS was performed on a FTIR spectrometer (Nicolet Nexus 670) equipped with a smart collector and MCT/A detector. Prior to experiments, the samples were pretreated at 150 °C for 60 min under He flow to remove adsorbed impurities. The background spectrum was collected under He and automatically deducted from the sample spectra. Afterward, gaseous toluene/He was introduced to the cell at a flow rate of 50 mL min<sup>-1</sup> at elevated temperature and DRIFTS spectra were recorded.

## 2.4. Photo-thermocatalytic activity

The photo-thermocatalytic activity of the samples for toluene oxidation was evaluated in a cylindrical stainless steel reactor with a quartz window under IR light irradiation (375 W, Philips) with an 800 nm cut-off filter. In the experiments, an ethanol suspension containing 0.1 g of the catalyst was prepared and coated on a fiberglass membrane of 50 mm diameter, dried at 60 °C and finally placed on the photoreactor. After IR irradiation for 10 min, the simulated air stream (21% O<sub>2</sub>/N<sub>2</sub>) containing 930 mg L<sup>-1</sup> of toluene passed through the catalyst layer (0.1 g) with a total flow rate of 51.8 mL min<sup>-1</sup>, giving a gas hourly space velocity (GHSV) of 31 080 mL (g<sup>-1</sup> h<sup>-1</sup>). The concentration of toluene and evolution of CO<sub>2</sub> were monitored by an on-line gas chromatograph equipped with two flame ionization detectors (FID) and a nickel-based methanizer. The toluene conversion and CO<sub>2</sub> yield for the photocatalytic reaction were calculated by using eqn (1) and (2), respectively.

$$\text{Toluene conversion (\%)} = 100\% \times ([\text{toluene}]_{\text{in}} - [\text{toluene}]_{\text{out}}) / [\text{toluene}]_{\text{in}} \quad (1)$$

$$\text{CO}_2 \text{ yield (\%)} = 100\% \times [\text{CO}_2]_{\text{produced}} / [\text{CO}_2]_{\text{theoretical}} \quad (2)$$

## 2.5. Photocatalytic activity

The procedure of measuring the photocatalytic activity of the catalyst for toluene oxidation with irradiation of an IR lamp is the same as that for photo-thermocatalytic activity described above, except for the following: 0.1 g catalyst powder was coated on the bottom of a cylindrical quartz reactor (5 cm × 5 cm × 1 cm). A thermocouple was put on the catalyst to measure its temperature. The photo-reactor was placed in a glycerol–water bath to keep the reaction temperature near room temperature (18 °C) under IR lamp irradiation.

## 2.6. Toluene adsorption experiment

The N<sub>2</sub> stream at 51.8 mL min<sup>-1</sup> containing 930 mg L<sup>-1</sup> of toluene passed through the catalyst layer (0.1 g) at various temperatures. The concentration of toluene before and after the adsorption process was measured by an on-line gas chromatograph equipped with FID.

# 3. Results and discussion

Crucially, the insight gained from theoretical and experimental work suggests that transition to rGO through chemical or thermal removal of oxygen in GO allows it to be reduced incrementally so that the infrared light absorption is significantly increased several fold.<sup>12,18,19</sup> Our one-step strategy for the synthesis of Pt-rGO hybrid proceeds *via* previously reported solvothermal reaction,<sup>13</sup> simultaneous reduction of GO and *in situ* loading of Pt NPs on rGO nanosheets. The XRD peak at around 39.7° for as-prepared Pt-rGO hybrid in Fig. 1(a) can be well indexed to the (111) diffraction peak of the Pt crystalline state with face-center-cubic structure. The typical peak of GO located at

around 10.2° is not observed, but the broad lump peak at around 24.5° corresponding to characteristic rGO is clearly observed. Moreover, the reduction of GO to rGO was further characterized by XPS. As displayed in Fig. 1(b), the deconvoluted C 1s peaks located at 284.6, 286.0, 288.2 and 290.2 eV are characteristic of C–C, C–O, C–O–C/C=O and COOH,<sup>15</sup> respectively. Notably, the peaks associated with C–C (284.6 eV) became predominant, while those associated with the oxidized carbon species were greatly weakened, indicating significant deoxygenation of oxygen-containing functional groups of GO. The characteristic peaks of Pt 4f<sub>5/2</sub> and Pt 4f<sub>7/2</sub> located at 71.7 eV and 75.0 eV are assigned to the core levels of Pt<sup>0</sup>.<sup>20</sup> Raman spectroscopy has been applied to distinguish the sp<sup>2</sup>/sp<sup>3</sup> hybridization and ordered/disordered carbon structures in carbonaceous materials.<sup>21</sup> As shown in Fig. 1(c), the Raman spectrum of Pt-rGO hybrid exhibits the prominent D band (~1350 cm<sup>-1</sup>) and G band (~1590 cm<sup>-1</sup>) of rGO, corresponding to the breathing mode of *k*-point phonons of A<sub>1g</sub> symmetry adjacent to a defect/edge and E<sub>2g</sub> phonons of C sp<sup>2</sup> atoms in a planar conjugated structure,<sup>22</sup> respectively. The Pt-rGO hybrid has an increased D/G intensity ratio relative to rGO, suggesting a decrease in the number of in-plane sp<sup>2</sup> domains and a partially ordered crystal structure in Pt-rGO hybrid due to potential interaction between Pt NPs and rGO nanosheets.<sup>23</sup> The SEM and HR-TEM images of Pt-rGO hybrid in Fig. 1(d) and (e) clearly show that rGO is a sheet-like structure with scrolling and corrugation, while Pt NPs are well dispersed, with a mean particle size of about 2.46 nm, on the external surface of rGO nanosheets. Therefore, XRD, XPS, Raman and HR-TEM characterizations together demonstrate that GO was effectively deoxygenated to form rGO nanosheets and uniform Pt NPs were successfully assembled on the surface of rGO nanosheets by means of solvothermal treatment. Pt-rGO hybrid appears black (Fig. S1†) and is stable under outdoor conditions. Moreover, the chemical stability of the Pt-rGO hybrid nanostructure in an air atmosphere at various temperatures was investigated by MS and TG. Under air atmosphere, the Pt-rGO hybrid is stable at temperatures up to 180 °C because (1) the signal of mass spectra presents that the carbon skeletons of rGO start to be broken down by combustion and enable the production of CO<sub>2</sub> at temperatures above 180 °C (Fig. S2(a)†); (2) TG displays a slight weight loss from room temperature to 400 °C (Fig. S2(b)†).

To experimentally evaluate the light absorption capacity, we measured the diffuse reflectance of Pt-rGO hybrid. As shown in Fig. 2 and Table 1, the Pt-rGO hybrid exhibits a prominent absorption feature over the whole range of the solar spectrum, with a total absorbance of 96.87% involving 93.38% of UV, 97.01% of visible, and 96.63% of infrared irradiation. The Pt-rGO–TiO<sub>2</sub> presents a similar absorption feature as the Pt-rGO, but with slightly decreased absorbance owing to the inefficient absorption in the vis-IR region of TiO<sub>2</sub>. Importantly, Pt-rGO hybrid shows absorption comparable with rGO through the whole solar spectrum and a similar zero-band-gap (Fig. S3†), indicating that Pt-decorated rGO nanosheets inherit the light absorption feature of rGO nanosheets, since the light absorption ability of Pt NPs is much weaker than that of rGO nanosheets. Significantly, Pt-rGO hybrid with such ultra-narrow band edge energy located in the infrared range would give rise

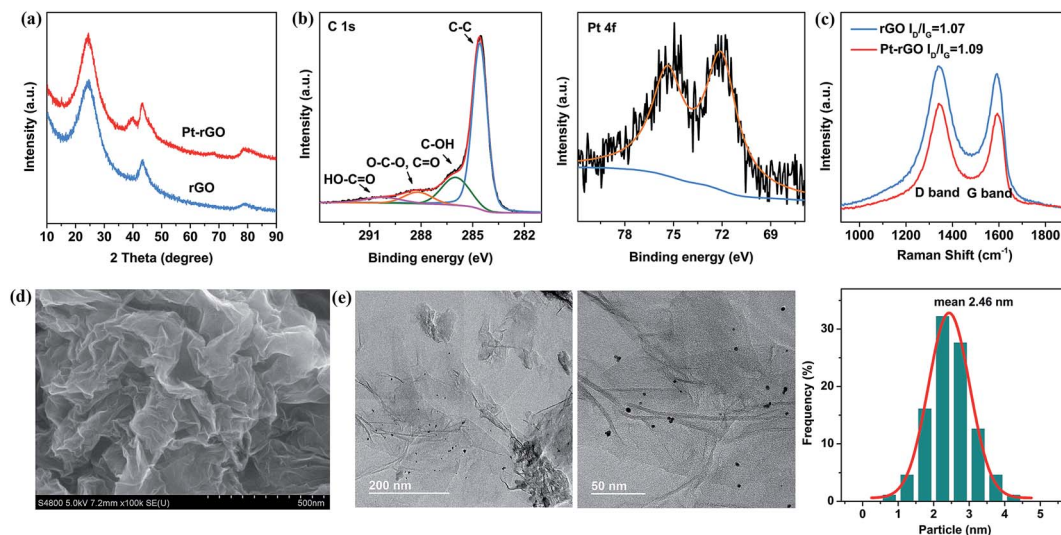


Fig. 1 (a) XRD patterns; (b) XPS spectra of C 1s and Pt 4f; (c) Raman spectra; (d) SEM image and (e) HR-TEM images of as-prepared Pt-rGO hybrid and the Pt NPs size distribution.

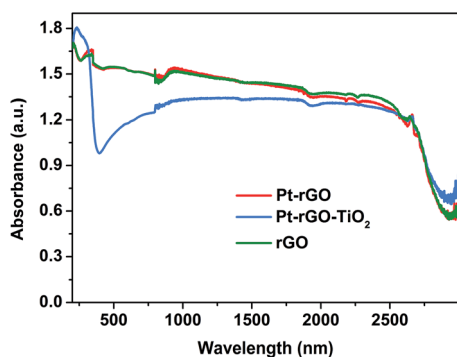


Fig. 2 DRS of rGO, Pt-rGO and Pt-rGO-TiO<sub>2</sub> composite.

to infinite heat generation through vibration of the crystal lattice<sup>11</sup> and is expected to be a promising material for the development of solar-thermal conversion.

Encouraged by the strong ultrabroad absorption band of Pt-rGO hybrid, IR light irradiation was employed to inspect its photothermal catalysis ability, such as for toluene oxidation. For IR illumination at 88, 115 and 146 mW cm<sup>-2</sup>, the catalytic toluene conversions over Pt-rGO hybrid are as high as 21.36%, 86.18% and 98.13% (Fig. 3(a)), respectively, and the catalytic mineralization values are 17.66%, 80.84% and 96.13% (Fig. 3(b)), respectively, ~9.28%, ~16.85% and ~8.71% higher than those of Pt-rGO-TiO<sub>2</sub> composite. The apparent activation energies ( $E_{app}$ ) based on Pt-rGO and Pt-rGO-TiO<sub>2</sub> are calculated to be 106.42 kJ mol<sup>-1</sup> and 123.90 kJ mol<sup>-1</sup> (Fig. 3(c)), respectively. Strikingly, the trend observed for catalytic performance is positively correlated with light intensity and greatly increases with light intensity increase. Specifically, the reaction temperature spontaneously increases from room temperature to 122 °C, 154 °C and 180 °C for Pt-rGO and to 116 °C, 147 °C and 176 °C for Pt-rGO-TiO<sub>2</sub> composite under IR irradiation

Table 1 Physical structural parameters of different samples

Sample	Pt-rGO	Pt-rGO-TiO <sub>2</sub>
$S_{BET}$ (m <sup>2</sup> g <sup>-1</sup> )	440.08	65.62
Pore volume (cm <sup>3</sup> g <sup>-1</sup> )	0.36	0.46
Pore size (nm)	1.47	3.93
Band gap (eV)	0	0, 2.94, 3.02
Pt loading (wt%) <sup>a</sup>	0.89	0.91
Absorbance (%) <sup>b</sup>	Solar	96.87
	UV	93.38
	Vis	97.01
	IR	96.63
Dynamic adsorption capacity of toluene (g L <sup>-1</sup> ) <sup>c</sup>	25 °C	193.54
	120 °C	50.14
	150 °C	36.65
	180 °C	27.61

<sup>a</sup> The value was obtained from ICP analysis. <sup>b</sup> Absorbance ( $a = \int(1 - R(\lambda)) \times E / \int E$ ,<sup>24,25</sup> solar: 300–2500 nm, UV: 300–400 nm, vis: 400–800 nm, IR: 800–2500 nm. <sup>c</sup> Dynamic adsorption capacity is integrated from breakthrough curves in Fig. 6(a).

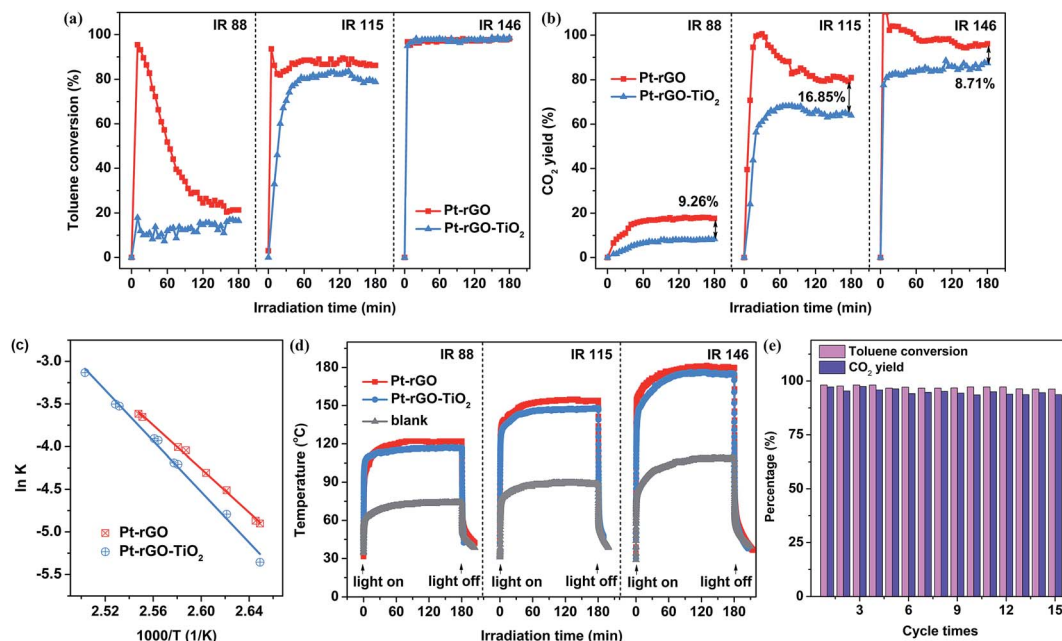


Fig. 3 (a) Time course of toluene conversion, (b) CO<sub>2</sub> yield, (c) linear-fitting Arrhenius plots of Pt-rGO and Pt-rGO-TiO<sub>2</sub> catalysts and (d) the corresponding temperature curves over Pt-rGO, Pt-rGO-TiO<sub>2</sub> and blank fiberglass membrane under IR irradiation at various light intensities (88, 115 and 146 mW cm<sup>-2</sup>); (e) the durability of Pt-rGO composite for toluene oxidation with IR irradiation of 146 mW cm<sup>-2</sup> under steady state conditions.

intensities of 88, 115 and 146 mW cm<sup>-2</sup> (Fig. 3(d)), respectively, evidently higher than the resulting temperature (74 °C, 89 °C, 108 °C) of the reaction system with fiberglass membrane but without catalyst coating. Importantly, the chemical stability measurement (Pt-rGO hybrid is highly stable in air atmosphere at temperatures up to 180 °C, Fig. S2†) together with the durability experiment (the amount of evolved CO<sub>2</sub> under catalytic reaction conditions is continuous and stable, Fig. S4†) rule out the possibility of carbon skeletons in rGO, confirming that the carbon source of reaction product CO<sub>2</sub> originated from the photothermal catalytic oxidation of C<sub>7</sub>H<sub>8</sub>. Likewise, as revealed by on-line GC and MS analyses shown in Fig. S4,† toluene catalysis experiments with oxygen atmosphere yielded the dominant product of CO<sub>2</sub>. However, under oxygen-free atmosphere, neither distinct degradation of toluene nor discernable generation of CO<sub>2</sub> can be clearly observed, which ascertained that the oxygen source of reaction product CO<sub>2</sub> derives from the extraction of oxygen from oxygen atmosphere for toluene oxidation reaction. Additionally, recycling experiments for Pt-rGO hybrid exhibit no noticeable change in the conversion and mineralization of toluene during 15 catalytic runs for 45 h under IR irradiation of 146 mW cm<sup>-2</sup> (Fig. 3(e)). Happily, as shown in Fig. S5 and Table S1,† Pt-rGO hybrid displays well-retained morphology, crystallinity and structural integrity from the XRD, SEM, HR-TEM and Raman measurements, with no oxidation of Pt and rGO nanosheets from XPS analysis after reaction, demonstrating its excellent recyclability and stability under light irradiation conditions. Furthermore, Pt-rGO hybrid has been shown to be active for the total oxidation of other common VOCs, such as isopropanol, acetone, *n*-hexane,

benzene, *o*-xylene. As displayed in Fig. S6,† conversion activity for this series of VOCs followed the sequence: benzene ≈ *o*-xylene > isopropanol > acetone > *n*-hexane > 74%; the mineralization activity order was as follows: isopropanol > acetone > *n*-hexane > benzene > *o*-xylene, indicating that Pt-rGO hybrid is a potential promising material available for oxidation of most emitted VOCs.

To differentiate the contributions of photoinduced hot hole driven photocatalysis or/and radiative heat transfer driven photo-thermocatalysis to the high catalytic activity, the steady-state temperature on the photocatalyst surface was measured *in situ* with a thermocouple during toluene oxidation. The reaction temperature was maintained at near room temperature by placing the reactor in a glycerol-water bath of ultralow temperature to eliminate the potential interference of photo-induced heat. After adsorption reaches saturation in 260 min at the temperature of 18 °C, neither distinct decrease in toluene concentration nor discernable increase in CO<sub>2</sub> concentration was clearly observed in the control experiments within 60 min under IR irradiation of 146 mW cm<sup>-2</sup> (Fig. S7†). This result indicates that the Pt-rGO hybrid is photocatalytically inactive toward toluene oxidation reaction at room temperature under light illumination, which can be ascribed mainly to: (1) the zero bandgap of rGO endowing the holes in the hybrid with inadequate oxidation capacity stemming from ungratified position-matching between the valence band of the semiconductor catalyst and the redox potentials of toluene species/active oxygen (<sup>•</sup>O<sub>2</sub><sup>-</sup> and <sup>•</sup>OH radicals) species, resulting in quick depletion of excitation energy *via* thermal radiative transfer; (2) nonexistence of energetic hot hole injections from the

excitation of Pt NPs with broad light absorption without a recognizable peak. As proved by the ESR spectra in Fig. S8,<sup>†</sup> neither  $\cdot\text{O}_2^-$  nor  $\cdot\text{OH}$  radical signal was detected in the IR-illuminated Pt-rGO suspension, indicating no reactive oxygen species generated from electronic excitation effect of Pt plasmon resonance and rGO. Previous works have established that the strong anisotropic bonding and low mass of the carbon atoms give graphene and graphene-based composites strong light absorption capability covering the full solar spectrum range,<sup>13,26–28</sup> where the strongly absorbed light radiation on Pt-rGO composite is efficiently converted into heat *via* electron-phonon and phonon-phonon processes. Thereby, rapid photothermal heating occurs on Pt-rGO hybrid upon light irradiation, resulting in a remarkable increase in the environmental temperature of the material.

Based on the above observations, we infer that photo-induced thermocatalysis is the decisive effect that catalyzes toluene oxidation. To further verify the temperature dependence of the reaction under various illumination conditions, the catalytic activity for toluene oxidation by irradiation of Pt-rGO hybrid with full spectrum, UV-vis or IR light was carried out. As displayed in Fig. 4, at identical temperature conditions illuminated by light with different wavelengths, the toluene conversion and  $\text{CO}_2$  yield over Pt-rGO hybrid for 150 min of full spectrum and UV-vis irradiation are almost equivalent to those

achieved with IR illumination. Significantly, Pt-rGO hybrid can effectively channel the flux of UV, vis and IR photons into heat to drive redox catalysis, with the photo-assisted catalytic process dominated solely by the photothermal effect of Pt-rGO hybrid without additional photoactivated charge transfer and injection. The photothermal conversion efficiency ( $\eta$ ) is defined by the ratio of the converted thermal energy *versus* the irradiation energy of photon flux,<sup>29</sup> where maximum solar-heat conversion efficiency is 17.6% for Pt-rGO composite under IR irradiation of  $146 \text{ mW cm}^{-2}$  (Fig. S9<sup>†</sup>).

Pt-rGO composite material shows great promise for redox reactions through photo-thermal effect in view of its efficient utilization of solar energy, which opens the possibility of emerging light-driven photo-thermocatalysis as an alternative to conventional electricity-driven thermal-based catalysis. To determine the origin of enhanced catalytic activity, especially mineralization, on Pt-rGO hybrid, we conducted a series of control experiments for performance comparison with Pt-rGO hybrid. As illustrated in Fig. S10,<sup>†</sup> rGO material initially exhibits almost complete toluene degradation in the first 5 minutes, but it gradually decreases with irradiation time and finally reduces to zero at 70 min or above under IR irradiation intensity of  $146 \text{ mW cm}^{-2}$ . This is because toluene adsorption is a fast process and equilibrium was reached in about 70 min for rGO material. Significantly, after adsorption of toluene to saturation, neither

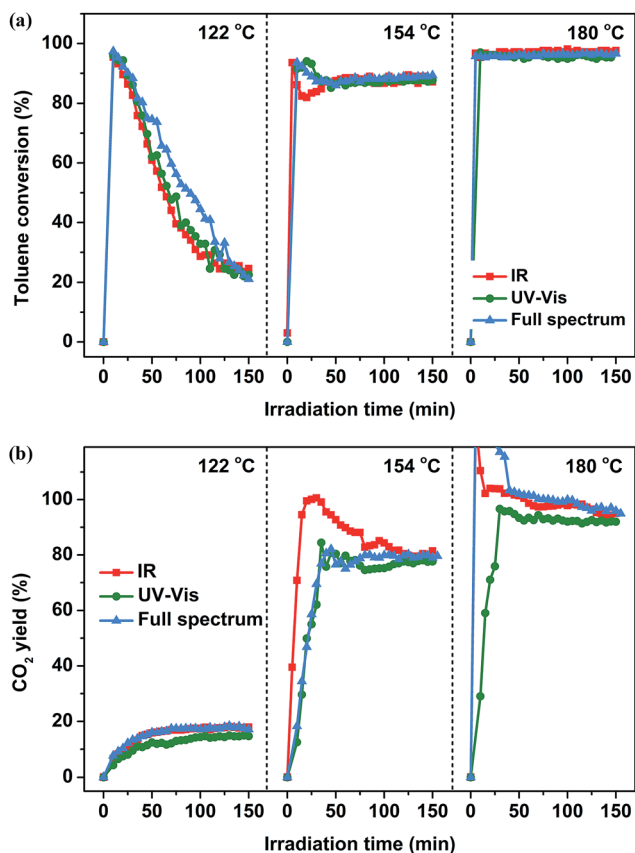


Fig. 4 (a) Time courses of toluene conversion and (b)  $\text{CO}_2$  yield over Pt-rGO composite modulated at identical temperatures under IR, UV-vis, full spectrum irradiation at various light intensities.

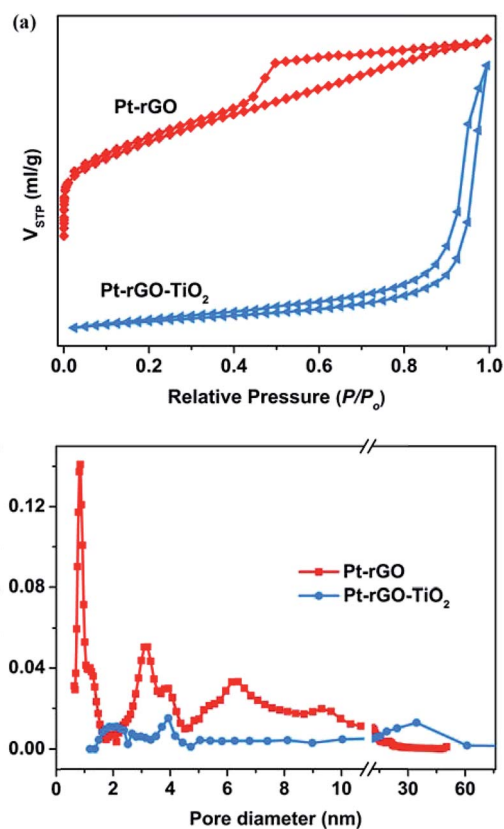


Fig. 5 (a) Nitrogen adsorption/desorption isotherms and (b) corresponding pore size distribution curves of Pt-rGO and Pt-rGO-TiO<sub>2</sub>.

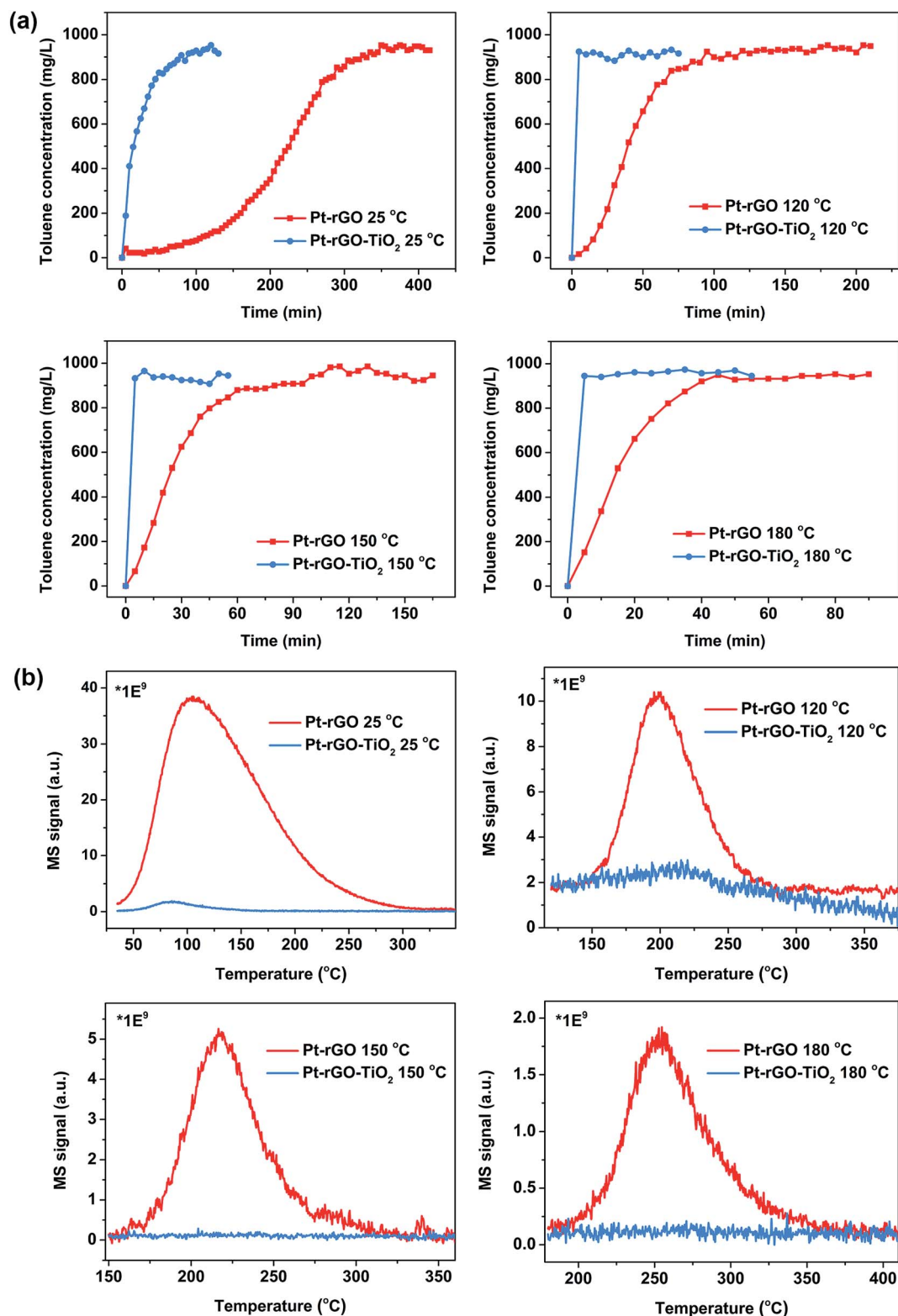


Fig. 6 (a) The breakthrough curves for adsorption (toluene concentration  $930 \text{ mg L}^{-1}$ , gas flow rate  $51.8 \text{ mL min}^{-1}$ , catalyst  $0.10 \text{ g}$ ) and (b) toluene-TPD over Pt-rGO and Pt-rGO-TiO<sub>2</sub> at various temperatures.

observable toluene degradation nor discernable CO<sub>2</sub> generation occur under IR illumination, even if the rGO itself displays strong IR light absorption and remarkable photothermal effect,

suggesting that no catalytic oxidative degradation of toluene can be achieved on rGO material, whose role would be not in the catalysis of this reaction but in proper positioning of the

adsorption layer. Importantly, Pt-decorated rGO nanosheets-adsorption layer exhibits significantly improved activity, highlighting that the photoinduced heat supplied to Pt active sites holds the key to the catalytic performance. The energy intensity of black rGO nanosheets was very high (absorptance of 97%), essentially independent of the Pt NPs' limited absorptance (67%) in this system. Herein, the Pt catalytic sites coordinated on rGO nanosheets serve as a highly active and durable heterogeneous catalyst for toluene oxidation, where the rGO provides homogeneous light absorption with Pt active sites for efficient heat transfer.

As described above, the Pt-rGO hybrid shows superior photothermal catalytic activity with even higher toluene conversion and mineralization efficiency than those of Pt-rGO-TiO<sub>2</sub> composite under light irradiation. For deeper insight into the performance enhancement of the Pt-rGO hybrid, multifarious combined characterizations, such as BET and toluene adsorption/desorption, were conducted to investigate the physicochemical properties of the material. The textural structure of Pt-rGO hybrid is examined by nitrogen physisorption measurement. As shown in Fig. 5(a), the adsorption-desorption isotherm shows a type IV isotherm with pronounced adsorptions at low (<0.1  $P/P_0$ ) and medium (0.2–0.9  $P/P_0$ ) relative pressures, indicating the existence of micropores and mesopores in rGO nanosheets.<sup>30</sup> Moreover, a very small hysteresis loop between the adsorption and desorption branches in the pressure range of 0.4–0.9  $P/P_0$  further reveals highly uniform pore size in porous rGO nanosheets. The pore size distribution curve (DFT model) derived from the adsorption branch in Fig. 5(b) clearly exhibits a dominant peak at 0.82 nm and several small peaks at 1.25, 3.11, 3.89, 6.32 and 9.33 nm. For the Pt-rGO-TiO<sub>2</sub> sample, the adsorption curve distinctly shows initial uptake in the low pressure range near 0.02, gradual increase of the volume adsorbed in the medium pressure range, and no saturation in the high pressure range, which indicates the existence of an extremely small number of micropores and various sizes of mesopores in a wide size distribution.<sup>31</sup> The hysteresis loop shifts to a higher and wider  $P/P_0$  pressure range (0.4–1.0  $P/P_0$ ), which is related to the presence of a wider range of mesopores with larger diameters.<sup>32</sup> The pore size distribution curve (BJH model) derived from the desorption branch clearly displays two narrow distributions of pores centered around 1.97 and 3.94 nm, as well as one broad distribution centered at approximately 34.10 nm, suggesting Pt-rGO-TiO<sub>2</sub> mainly consists of mesoporous structure. The pore parameters and BET surface areas are summarized in Table 1. Significantly, the adsorption data of Pt-rGO hybrid indicate a very high specific surface area of 440.08 m<sup>2</sup> g<sup>-1</sup>. In most cases, a support with large specific surface area helps increase the exposed active surface sites of metal loading for gas absorption and catalytic surface reactions,<sup>33</sup> thus promoting the injection of activated oxygen atoms to adsorbed toluene and improving catalyst efficiency. The size distribution histogram of the Pt NPs in Pt-rGO hybrid, created by randomly choosing 100 black dots from HR-TEM images in Fig. 1(e), exhibits that the average size of the well-dispersed Pt NPs is 2.46 nm, smaller than that in Pt-rGO-TiO<sub>2</sub>.

In principle, both adsorption and catalytic oxidation could decrease toluene concentration. Before the catalytic oxidation, the dynamic adsorption behavior of Pt-rGO and Pt-rGO-TiO<sub>2</sub> samples for gaseous toluene at a concentration of 930 mg L<sup>-1</sup> in a N<sub>2</sub> stream was measured by an on-line gas chromatograph equipped with FID. Fig. 6(a) presents the evolution of toluene outlet concentration as a function of time at different temperatures. At the beginning of the breakthrough curve for Pt-rGO, the toluene outlet concentration is nil, which means that all gaseous toluene is completely adsorbed, indicating good adsorption capacity at saturation. One can also observe that breakthrough occurs more rapidly on Pt-rGO-TiO<sub>2</sub>; after only a few minutes, toluene outlet concentration rises to initial concentration. Adsorption is closely related to temperature, as almost no obvious toluene adsorption occurs on Pt-rGO-TiO<sub>2</sub> at temperatures of 120 °C or above, but toluene adsorption capacities over Pt-rGO hybrid are as high as 193.54, 50.14, 36.65 and 27.61 g L<sup>-1</sup> at the temperature of 25, 120, 150 and 180 °C, respectively, much higher than those obtained with the Pt-rGO-TiO<sub>2</sub> composite. Under identical conditions, Pt-rGO hybrid shows superior adsorption ability compared with Pt-rGO-TiO<sub>2</sub> composite. Specifically, gaseous toluene is retained on Pt-rGO longer than on Pt-rGO-TiO<sub>2</sub>, which is consistent with toluene-TPD in Fig. 6(b). Dramatically, the toluene adsorption capacity of the catalysts follows the same trend as  $S_{\text{BET}}$ . Previous reports have also shown that surface area determines adsorption capacity for either microporous or mesoporous materials.<sup>34</sup> However, even after eliminating the direct effect of surface area through normalization, the adsorption capacity of Pt-rGO hybrid is still much higher than that of Pt-rGO-TiO<sub>2</sub> composite, revealing the strong superiority of microporous Pt-rGO. This observation is specifically associated with different adsorption potentials of micropores and mesopores in catalysts, where the adsorption potentials from adjacent micropore walls can be stacked and thus promote adsorption of gaseous toluene on the catalyst surface, while the adsorption potential in mesopores is significantly shallower due to the large pore size.<sup>35</sup> Given the strong adsorption potential in micropores, either the reactant adsorbed or intermediate mineralization formed in micropores during catalytic oxidation is relatively difficult to release and stays a considerable time on the catalyst surface.<sup>36</sup> Unsurprisingly, rGO possesses a large delocalized sp<sup>2</sup> carbon structure, endowing it with good adsorption efficiency towards reactants with a conjugate aromatic structure, mainly *via*  $\pi$ - $\pi$  cooperative interactions. Moreover, the effective site of the sp<sup>2</sup> carbon of rGO has abundant free-flowing  $\pi$  electrons and can be activated by conjugation with the long pair electrons from the loaded Pt atoms, simultaneously increasing the  $\pi$ - $\pi$  interaction. As a result, the adsorption capacity of Pt-rGO hybrid toward toluene is increased by the  $\pi$ - $\pi$  interaction, which increases the number of activated toluene molecules. The above analysis reveals that such conspicuous adsorption capacity of Pt-rGO hybrid is predominantly ascribed to the strong affinity between the toluene molecules and the surface of Pt-rGO hybrid, deriving from its extremely large surface area, abundant micropore structure and highly strong  $\pi$ - $\pi$  interaction. As presented in Fig. 1, the photothermal catalytic activity of Pt-rGO

greatly improved with higher rGO content in comparison to that of Pt-rGO-TiO<sub>2</sub>-TiO<sub>2</sub>, achieving approximately 8–17% enhancement of mineralization efficiency. This highlighted that the low rGO content in the Pt-rGO-TiO<sub>2</sub> sample did not provide adequate adsorption capacity to suppress accumulation of carbonaceous intermediates, resulting in decreased toluene mineralization. However, upon increasing the rGO content, the intimate contact area and resulting prolonged interfacial interaction between catalyst and reactant enable the adsorbed toluene/intermediates to sufficiently react with oxygen to generate the end products of CO<sub>2</sub> and H<sub>2</sub>O.

To reveal more details of catalytic toluene oxidation over Pt-rGO hybrid, *in situ* DRIFTS spectroscopy was performed to explore the evolved surface chemical species. Prior to toluene

adsorption and reaction experiments, the Pt-rGO catalyst was flushed with high-purity He at 150 °C for 1 h to remove adsorbed impurities. The background spectrum was collected and automatically deducted from the sample spectra. Then, a flow of toluene/20% O<sub>2</sub>/He feed gas was introduced to the cell at a flow rate of 50 mL min<sup>-1</sup>. Afterwards, a series of DRIFTS spectra were recorded at an elevated temperature. As displayed in Fig. 7, the broad peaks at 3084, 3039 and 2961 cm<sup>-1</sup> are assigned to C–H stretching vibrations of the aromatic ring, while those at 2917 and 2870 cm<sup>-1</sup> are attributed to asymmetric and symmetric C–H stretching vibrations of the methyl group,<sup>37</sup> respectively. The weak band at 1256 cm<sup>-1</sup> is characteristic of ring vibrations.<sup>38</sup> These absorption peaks from the adsorbed toluene develop rapidly and reach a steady level within a few minutes. An intense peak at 1180 cm<sup>-1</sup> with a small shoulder at 1084 cm<sup>-1</sup> corresponds to C–O stretching vibration of an alkoxide species.<sup>39</sup> The peak at 954 cm<sup>-1</sup> is associated with the bending and torsional vibrations of CH<sub>2</sub>.<sup>40</sup> The appearance of these absorption peaks suggests that the C–H bond of the methyl group of an aromatic ring is cleaved to generate C–O bonds, where the O atoms come from dissociated pre-adsorbed O<sub>2</sub> molecules on Pt NPs decorated rGO nanosheets, forming a benzoyl species (C<sub>6</sub>H<sub>5</sub>-CH<sub>2</sub>-O).<sup>41</sup> The new doublet peaks at 2362 and 2341 cm<sup>-1</sup> are characteristic of asymmetric O=C=O stretching vibrations<sup>42,43</sup> and the intensities of their peaks drastically increase with temperature, owing to the contribution of more generated CO<sub>2</sub> as final product during progressively deeper catalytic oxidation reactions of adsorbed toluene species at a higher temperature.

To further validate the degradation mechanism, the deposits on used Pt-rGO hybrid (illuminated in a continuous flow of 7254 mg L<sup>-1</sup> toluene/21% O<sub>2</sub>/N<sub>2</sub> feed gas with IR light intensity

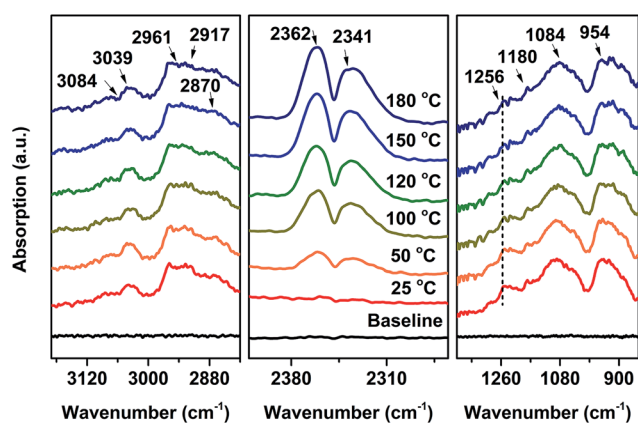


Fig. 7 *In situ* DRIFTS spectra of adsorbed species on Pt-rGO hybrid in a continuous toluene/air feed gas upon heating at an elevated temperature.

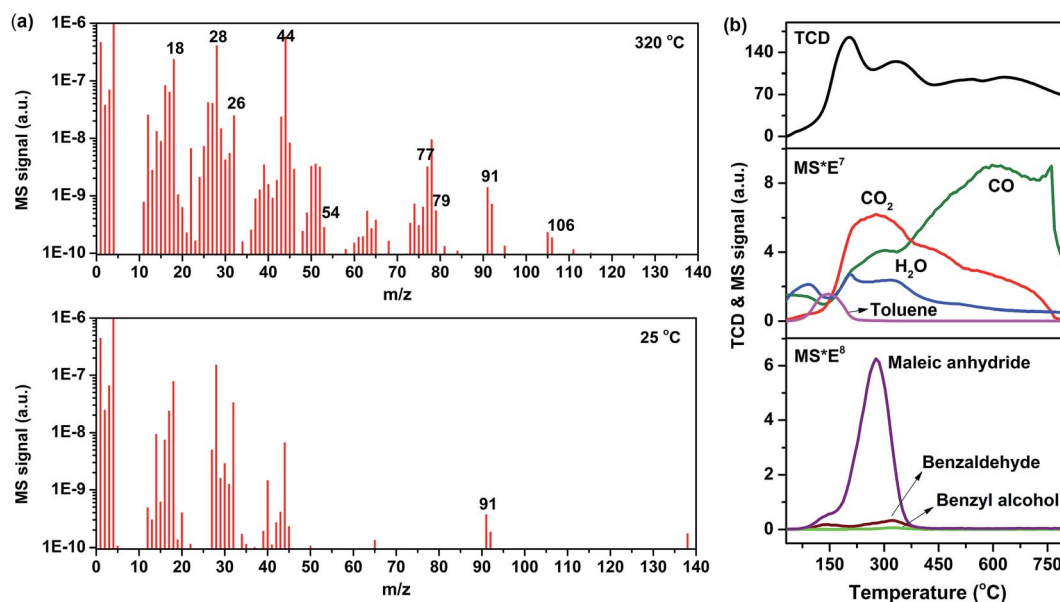
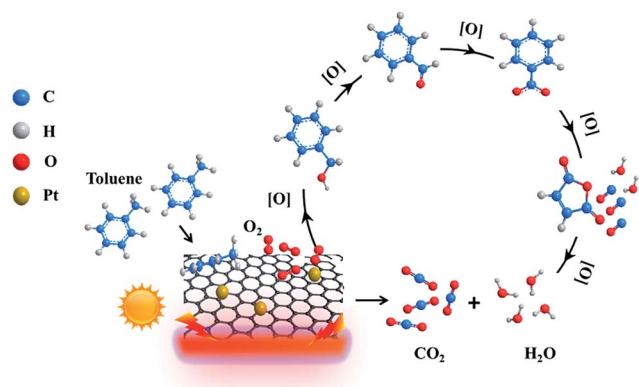


Fig. 8 (a) On-line TPD-MS result for used Pt-rGO hybrid illuminated with IR light intensity of 88 mW cm<sup>-2</sup> under a continuous flow of 7254 mg L<sup>-1</sup> toluene/21% O<sub>2</sub>/N<sub>2</sub> feed gas for 60 h; (b) the released species in the outlet gas, containing CO<sub>2</sub> ( $m/z = 44$ ), CO ( $m/z = 28$ ), H<sub>2</sub>O ( $m/z = 18$ ), toluene ( $m/z = 92, 91, 65, 63, 39$ ), benzyl alcohol ( $m/z = 79$ ), benzaldehyde ( $m/z = 77, 106$ ) and maleic anhydride ( $m/z = 54, 26$ ).



Scheme 1 Proposed reaction pathway for photo-thermal catalytic oxidation of toluene on Pt-rGO hybrid.

of  $88 \text{ mW cm}^{-2}$  for 60 h) were investigated using temperature-programmed desorption coupled with mass spectrometry detection (TPD-MS). 600 mg of used Pt-rGO hybrid was loaded in a U-shaped quartz tube, installed in a furnace coupled to a temperature controller-programmer and exposed to a He flow at  $30 \text{ mL min}^{-1}$  for 20 min to remove  $\text{O}_2$  from the system. The temperature was then raised from room temperature to  $810 \text{ }^\circ\text{C}$  at a rate of  $10 \text{ }^\circ\text{C min}^{-1}$  and the effluents were analyzed by thermal conductivity (TCD) and MS (Tilon, TC-D200 M). The signals at mass to charge ( $m/z$ ) ratios were recorded from 0 to 180, as shown in Fig. S1.† Signals for  $m/z = 44$  ( $\text{CO}_2$ ),  $m/z = 28$  ( $\text{CO}$ ; relative contributions of residual  $\text{N}_2$  and  $\text{CO}_2$  fragmentation characteristic to the overall 28 signal were indistinct),  $m/z = 18$  ( $\text{H}_2\text{O}$ ),  $m/z = 54$  (maleic anhydride),  $m/z = 79$  (benzyl alcohol),  $m/z = 77$  (benzaldehyde) and  $m/z = 91$  (toluene) were monitored by on-line MS during the TPD experiment, as displayed in Fig. 8. In the compositional analysis of the effluent gas, benzyl alcohol, benzaldehyde and maleic anhydride were identified as reaction intermediates resulting from partial oxidation of toluene. Under light irradiation, photo-thermal responsive Pt-rGO composite achieves broad spectrum utilization for thermalization, where the generated heat increases the local temperature of the system and thus triggers the toluene catalytic oxidation reaction. On the Pt-rGO catalyst, pre-adsorbed  $\text{O}_2$  molecules are first dissociated on Pt NPs-decorated rGO nanosheets to form activated O atoms, subsequently spill to the surface of rGO nanosheets, and actively react with the chemisorbed toluene molecules, giving intermediates of benzoyl, benzoate and maleic anhydride species. Finally, the adsorbed maleic anhydride is further oxidized by activated O atoms to the final products of  $\text{CO}_2$  and  $\text{H}_2\text{O}$  (Scheme 1).

## 4. Conclusion

We constructed large-area contiguous rGO nanosheets adsorption layer supported Pt NPs with surprisingly high infrared absorption, well-dispersed active Pt nanoparticles and strong reactant adsorption capacity with light irradiation. Such unique properties lead to high light-mediated activity of Pt-rGO hybrid for typical catalytic reaction through photo-thermal effect,

giving a toluene conversion of 98% and  $\text{CO}_2$  yield of 96% under an IR irradiation intensity of  $146 \text{ mW cm}^{-2}$ , together with remarkable stability. Comparative characterizations disclose that the synergistic effects of ultrabroadband strong light absorption, efficient light-to-heat conversion, considerably high adsorption ability and preferentially exposed catalytically active sites enable significantly improved performance. Research efforts in this direction could potentially provide a new strategy to effectively utilize solar energy in a wide range of chemical reactions.

## Conflicts of interest

There are no conflicts to declare.

## Acknowledgements

This work was supported by the One Hundred Talent Project and the Key Program for Frontier Sciences from Chinese Academy of Sciences [QYZDB-SSWDQC022]; National Natural Science Foundation of China [No. 21703233]; “Cooperation of Industry-University-Institute and Scientific and Technological Cooperation” of Xiamen [No. 3502Z20182006].

## Notes and references

- 1 P. Christopher, H. L. Xin and S. Linic, *Nat. Chem.*, 2011, **3**, 467–472.
- 2 N. Armaroli and V. Balzani, *Angew. Chem., Int. Ed.*, 2007, **46**, 52–66.
- 3 G. W. Crabtree and N. S. Lewis, *Phys. Today*, 2007, **60**, 37–42.
- 4 H. Y. Ren, M. Tang, B. L. Guan, K. X. Wang, J. W. Yang, F. F. Wang, M. Z. Wang, J. Y. Shan, Z. L. Chen, D. Wei, H. L. Peng and Z. F. Liu, *Adv. Mater.*, 2017, **29**, 1702590–1702596.
- 5 J. D. Yao, Z. Q. Zheng and G. W. Yang, *Nanoscale*, 2018, **10**, 2876–2886.
- 6 S. Paterson, S. A. Thompson, A. W. Wark and R. de la Rica, *J. Phys. Chem. C*, 2017, **121**, 7404–7411.
- 7 G. Z. Jia, P. Wang, Y. B. Zhang and K. Chang, *Sci. Rep.*, 2016, **6**, 25884–25891.
- 8 R. Marasini, A. Pitchaimani, T. D. T. Nguyen, J. Comer and S. Aryal, *Nanoscale*, 2018, **10**, 13684–13693.
- 9 J. J. Qiu and W. D. Wei, *J. Phys. Chem. C*, 2014, **118**, 20735–20749.
- 10 D. M. Schultz and T. P. Yoon, *Science*, 2014, **343**, 985–994.
- 11 J. Wang, Y. Li, L. Deng, N. Wei, Y. Weng, S. Dong, D. Qi, J. Qiu, X. Chen and T. Wu, *Adv. Mater.*, 2017, **29**, 1603730–1603735.
- 12 M. Acik, G. Lee, C. Mattevi, M. Chhowalla, K. Cho and Y. J. Chabal, *Nat. Mater.*, 2010, **9**, 840–845.
- 13 J. J. Li, S. C. Cai, E. Q. Yu, B. Weng, X. Chen, J. Chen, H. P. Jia and Y. J. Xu, *Appl. Catal., B*, 2018, **233**, 260–271.
- 14 C. H. Bartholomew, *Appl. Catal., A*, 2001, **212**, 17–60.
- 15 Y. Zhang, N. Zhang, Z.-R. Tang and Y.-J. Xu, *J. Phys. Chem. C*, 2014, **118**, 5299–5308.

- 16 Y. H. Zhang, Z. R. Tang, X. Z. Fu and Y. J. Xu, *ACS Nano*, 2010, **4**, 7303–7314.
- 17 X. M. Chen, B. Y. Su, G. H. Wu, C. J. Yang, Z. X. Zhuang, X. R. Wang and X. Chen, *J. Mater. Chem.*, 2012, **22**, 11284–11289.
- 18 K.-Q. Lu, N. Zhang, C. Han, F. Li, Z. Chen and Y.-J. Xu, *J. Phys. Chem. C*, 2016, **120**, 27091–27103.
- 19 M. Hashemi, M. Omid, B. Muralidharan, H. Smyth, M. A. Mohagheghi, J. Mohammadi and T. E. Milner, *ACS Appl. Mater. Interfaces*, 2017, **9**, 39872.
- 20 L. Pastor-Perez, V. Belda-Alcazar, C. Marini, M. M. Pastor-Blas, A. Sepulveda-Escribano and E. V. Ramos-Fernandez, *Appl. Catal., B*, 2018, **225**, 121–127.
- 21 Z. Chen, S. Q. Liu, M. Q. Yang and Y. J. Xu, *ACS Appl. Mater. Interfaces*, 2013, **5**, 4309–4319.
- 22 S. J. Guo, D. Wen, Y. M. Zhai, S. J. Dong and E. K. Wang, *ACS Nano*, 2010, **4**, 3959–3968.
- 23 J. L. Wang, G. K. Zhang and P. Y. Zhang, *Appl. Catal., B*, 2018, **239**, 77–85.
- 24 D. Q. Gong, H. D. Liu, G. Luo, P. Zhang, X. D. Cheng, B. Yang, Y. B. Wang, J. Min, W. X. Wang, S. P. Chen, Z. Q. Cui, K. W. Li and L. F. Hu, *Sol. Energy Mater. Sol. Cells*, 2015, **136**, 167–171.
- 25 M. Gao, P. K. N. Connor and G. W. Ho, *Energy Environ. Sci.*, 2016, **9**, 3151–3160.
- 26 A. A. Balandin, *Nat. Mater.*, 2011, **10**, 569–581.
- 27 Y. W. Zhu, S. Murali, W. W. Cai, X. S. Li, J. W. Suk, J. R. Potts and R. S. Ruoff, *Adv. Mater.*, 2010, **22**, 5226.
- 28 E. Pop, V. Varshney and A. K. Roy, *MRS Bull.*, 2012, **37**, 1273–1281.
- 29 M. Mao, Y. Li, J. Hou, M. Zeng and X. Zhao, *Appl. Catal., B*, 2015, **174**, 496–503.
- 30 S. B. Yang, X. L. Feng, L. Wang, K. Tang, J. Maier and K. Mullen, *Angew. Chem., Int. Ed.*, 2010, **49**, 4795–4799.
- 31 H. B. Li, L. K. Pan, T. Lu, Y. K. Zhan, C. Y. Nie and Z. Sun, *J. Electroanal. Chem.*, 2011, **653**, 40–44.
- 32 Y. L. Li, J. J. Wang, X. F. Li, D. S. Geng, R. Y. Li and X. L. Sun, *Chem. Commun.*, 2011, **47**, 9438–9440.
- 33 L. Huang, X. Hu, S. Yuan, H. Li, T. Yan, L. Shi and D. Zhang, *Appl. Catal., B*, 2017, **203**, 778–788.
- 34 A. A. Ismail and D. W. Bahnemann, *J. Mater. Chem.*, 2011, **21**, 11686–11707.
- 35 J. Lyu, L. Zhu and C. Burda, *ChemCatChem*, 2013, **5**, 3114–3123.
- 36 J. Z. Lyu, J. X. Gao, M. Zhang, Q. Fu, L. N. Sun, S. Hu, J. B. Zhong, S. Wang and J. Li, *Appl. Catal., B*, 2017, **202**, 664–670.
- 37 F. Zhang, M. J. Wang, X. D. Zhu, B. Hong, W. D. Wang, Z. M. Qi, W. Xie, J. J. Ding, J. Bao, S. Sun and C. Gao, *Appl. Catal., B*, 2015, **170**, 215–224.
- 38 X. Y. Wang, Y. Liu, T. H. Zhang, Y. J. Luo, Z. X. Lan, K. Zhang, J. C. Zuo, L. L. Jiang and R. H. Wang, *ACS Catal.*, 2017, **7**, 1626–1636.
- 39 Z. R. Zhu, F. Y. Liu and W. Zhang, *Mater. Res. Bull.*, 2015, **64**, 68–75.
- 40 V. Augugliaro, H. Kisch, V. Loddo, M. J. Lopez-Munoz, C. Marquez-Alvarez, G. Palmisano, L. Palmisano, F. Parrino and S. Yurdakal, *Appl. Catal., A*, 2008, **349**, 189–197.
- 41 H. Sun, Z. G. Liu, S. Chen and X. Quan, *Chem. Eng. J.*, 2015, **270**, 58–65.
- 42 X. Wang, H. Shi, J. H. Kwak and J. Szanyi, *ACS Catal.*, 2015, **5**, 6337–6349.
- 43 W. C. Wilfong, C. S. Srikanth and S. S. C. Chuang, *ACS Appl. Mater. Interfaces*, 2014, **6**, 13617–13626.